

# Nanoscale

Accepted Manuscript

This article can be cited before page numbers have been issued, to do this please use: T. Song, H. Tan, S. Estandía, J. Gazquez, M. Gich, N. Dix, I. Fina and F. Sanchez, *Nanoscale*, 2022, DOI: 10.1039/D1NR06983G.



This is an Accepted Manuscript, which has been through the Royal Society of Chemistry peer review process and has been accepted for publication.

Accepted Manuscripts are published online shortly after acceptance, before technical editing, formatting and proof reading. Using this free service, authors can make their results available to the community, in citable form, before we publish the edited article. We will replace this Accepted Manuscript with the edited and formatted Advance Article as soon as it is available.

You can find more information about Accepted Manuscripts in the [Information for Authors](#).

Please note that technical editing may introduce minor changes to the text and/or graphics, which may alter content. The journal's standard [Terms & Conditions](#) and the [Ethical guidelines](#) still apply. In no event shall the Royal Society of Chemistry be held responsible for any errors or omissions in this Accepted Manuscript or any consequences arising from the use of any information it contains.

## ARTICLE

**Improved polarization and endurance in ferroelectric  $\text{Hf}_{0.5}\text{Zr}_{0.5}\text{O}_2$  films on  $\text{SrTiO}_3(110)$ †**Tingfeng Song,<sup>a</sup> Huan Tan,<sup>a</sup> Saúl Estandía,<sup>a</sup> Jaume Gàzquez,<sup>a</sup> Martí Gich,<sup>a</sup> Nico Dix,<sup>a</sup> Ignasi Fina,<sup>\*a</sup> and Florencio Sánchez<sup>\*a</sup>Received 00th January 20xx,  
Accepted 00th January 20xx

DOI: 10.1039/x0xx00000x

The metastable orthorhombic phase of  $\text{Hf}_{0.5}\text{Zr}_{0.5}\text{O}_2$  (HZO) can be stabilized in thin films on  $\text{La}_{0.67}\text{Sr}_{0.33}\text{MnO}_3$  (LSMO) buffered (001)-oriented  $\text{SrTiO}_3$  (STO) by an intriguing epitaxy that results in (111)-HZO oriented growth and robust ferroelectric properties. Here, we show that the orthorhombic phase can also be epitaxially stabilized on LSMO/STO(110), presenting the same out-of-plane (111) orientation but a different distribution of in-plane crystalline domains. The remanent polarization of HZO films with a thickness of less than 7 nm on LSMO/STO(110) is  $33 \mu\text{C cm}^{-2}$ , which corresponds to a 50% improvement over equivalent films on LSMO/STO(001). Furthermore, HZO on LSMO/STO(110) presents higher endurance, switchable polarization is still observed up to  $4 \times 10^{10}$  cycles, and retention of more than 10 years. These results demonstrate that tuning epitaxial growth of ferroelectric  $\text{HfO}_2$ , here by using STO(110) substrates, allows improving functional properties of relevance for memory applications.

**1. Introduction**

The discovery of a ferroelectric phase of  $\text{HfO}_2$ ,<sup>1</sup> with robust properties at room temperature and compatibility with CMOS technology, has renewed the interest of the industry on ferroelectric memories. The different properties of ferroelectric  $\text{HfO}_2$  respect to conventional ferroelectrics have raised fundamental questions and may open up new applications. Ten years after the discovery of ferroelectric  $\text{HfO}_2$ , these different properties are still far from being fully understood. They can depend to a great extent on point defects, parasitic phases, interfaces with electrodes and between grains, crystal orientation, and lattice strain. Unraveling the relative contribution of these factors to the ferroelectric properties is hampered by the highly complex microstructure of the doped  $\text{HfO}_2$  films. Epitaxial films are more convenient than polycrystalline samples to advance towards this knowledge.<sup>2–7</sup> Significant progress has recently been made by studying epitaxial films of doped  $\text{HfO}_2$  on  $\text{La}_{0.67}\text{Sr}_{0.33}\text{MnO}_3$  (LSMO) buffered (001)-oriented  $\text{SrTiO}_3$  (STO) substrates. Relevant findings reported with epitaxial films include: demonstration of high polarization, endurance and retention in films less than 5

nm;<sup>8</sup> proof of ferroelastic domain switching;<sup>9</sup> demonstration of thickness ( $t$ ) dependence on the coercive electric field ( $E_c$ ) according to  $E_c - t^{-2/3}$  scaling;<sup>8,10–12</sup> estimation of the Curie temperature by X-ray diffraction measurements;<sup>13</sup> control of the relative amount of ferroelectric and paraelectric phases by substrate selection;<sup>14</sup> and improvement of the endurance in presence of parasitic monoclinic phase.<sup>15</sup>

Epitaxial growth can facilitate the strain control of functional properties. This is demonstrated for perovskite ferroelectrics on perovskite substrates,<sup>16,17</sup> but the epitaxial growth of fluorite ferroelectrics on perovskite substrates is much less flexible. Probably because due to the large structural difference between  $\text{HfO}_2$  and perovskite substrates, epitaxy occurs by the so-called domain matching epitaxy mechanism,<sup>18</sup> which results in a non-significant change of the lattice parameters of the  $\text{HfO}_2$  by changing the lattice mismatch via appropriate substrate selection.<sup>10,14</sup> Furthermore, the orthorhombic phase grows epitaxially on LSMO and other La-doped manganites, but not on other popular oxide electrodes such as  $\text{SrRuO}_3$ ,  $\text{LaNiO}_3$  or  $\text{La:BaSnO}_3$ .<sup>19</sup> These facts limit the possibilities of controlling the microstructure and the ferroelectric properties of epitaxial  $\text{HfO}_2$  films. Aiming to open new ways of control, we have investigated the growth of  $\text{Hf}_{0.5}\text{Zr}_{0.5}\text{O}_2$  (HZO) films on STO(110) substrates buffered with LSMO electrodes. The films are epitaxial and (111) oriented like equivalent films on STO(001), but they present a different set of in-plane crystal variants. We observe that this different crystalline microstructure has impact on functional properties, i.e. ferroelectric polarization is very high, around  $33 \mu\text{C cm}^{-2}$  in films less than 7 nm thick, representing an increase of 50% over equivalent films on STO(001). Films grown on STO(110) can be cycled with reduced electrical strength because the higher polarization, which allows enhancing the endurance up to  $4 \times 10^{10}$  cycles.

<sup>a</sup> Institut de Ciència de Materials de Barcelona (ICMAB-CSIC), Campus UAB, Bellaterra 08193, Barcelona, Spain. E-mail: ifina@icmab.es, fsanchez@icmab.es

†Electronic Supplementary Information (ESI) available: Simulation of Laue oscillations. Piezoresponse force microscopy amplitude images. Sketches of the epitaxial relationships between crystal variants and substrates. STEM: Simultaneous ABF and HAADF images. Top view of HZO(111) on LSMO(110). STEM characterization (Reconstructed image from reflections in the Fourier space). Atomic force microscopy image of the HZO/LSMO/STO(110) sample. Leakage curves during endurance tests. Polarization loops during endurance tests. See DOI: 10.1039/x0xx00000x



## 2. Experimental

HZO films were grown on LSMO buffered STO(001) and STO(110) substrates by pulsed laser deposition (PLD) using a KrF excimer laser. HZO films ( $t = 6.5$  nm) and LSMO electrodes ( $t = 25$  nm) were grown in a single process. HZO was deposited at optimal growth conditions: laser frequency 2 Hz, dynamic oxygen pressure of 0.1 mbar, and substrate temperature (heater block temperature) of 800 °C.<sup>10,20</sup> Films were cooled at the end of the deposition under 0.2 mbar oxygen pressure. Platinum circular top electrodes, of diameter 20  $\mu\text{m}$  and thickness 20 nm, were deposited ex-situ at room temperature by sputtering through stencil masks.

Crystal phase identification and epitaxy characterization was performed by X-ray diffraction (XRD) with Cu K $\alpha$  radiation using a Siemens D5000 diffractometer equipped with point detector, and a Bruker D8-Advance diffractometer equipped with 2D detector. Microstructural characterization was done by scanning transmission electron microscopy using a JEOL ARM 200CF STEM with a cold field emission source, equipped with a CEOS aberration corrector and operated at 200 kV. Film topography was analyzed using atomic force microscopy (AFM) using a Keysight 5100. Ferroelectric characterization was carried out using an AixACCT TFAAnalyser2000 platform. Polarization loops were measured at 1 kHz by the dynamic leakage current compensation (DLCC)<sup>21</sup> procedure at room temperature in top-bottom configuration, with the bottom LSMO electrode grounded. Residual leakage and series resistance contributions were subtracted using the reported methodology.<sup>22</sup> Endurance was measured at room temperature cycling the sample at frequency of 100 kHz using bipolar square pulses of indicated amplitude and measuring polarization loops at 1 kHz. Retention was measured at 85 °C, poling the sample by a triangular pulse of 0.25 ms and determining the remanent polarization from the first polarization curve of the polarization loop measured at 1 kHz using the positive up negative down protocol after a delay time. Piezoelectric force microscopy (PFM) measurements were performed with an MFP-3D microscope (Oxford Instrument Co.) using the BudgetSensors silicon (n-type) cantilevers with Pt coating (Multi75E-G). To achieve better sensitivity, the dual AC resonance tracking (DART) method was employed.<sup>23</sup> PFM voltage hysteresis loops were always performed at remanence using a dwell time of 100 ms. Due to the difficulties quantifying PFM response in DART, piezoelectric coefficients have not been evaluated, but all the measurements in the characterized samples are done under the same conditions, making them comparable.

## 3. Results

Fig. 1a shows the XRD  $\theta$ - $2\theta$  scans of the HZO/LSMO films on STO(001) (black line) and STO(110) (red line). The highest intensity peaks are STO reflections, and the shoulders at the right of these peaks are the corresponding LSMO reflections (LSMO grows with cube-on-cube epitaxial relationship on STO).

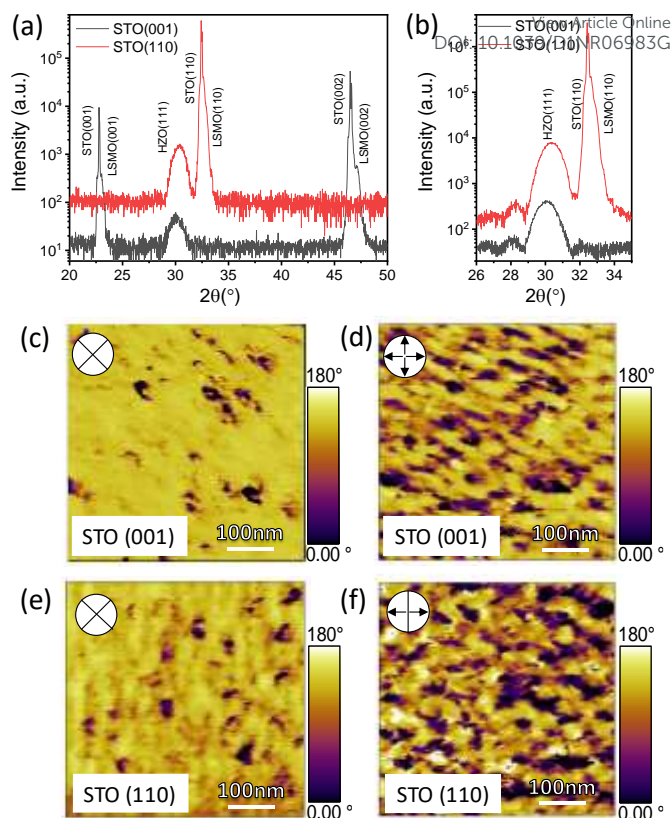


**Fig. 1** (a) XRD  $\theta$ - $2\theta$  scan of the HZO/LSMO/STO(001) (black line) and HZO/LSMO/STO(110) (red line) samples. (b) Zoomed scans, recorded with longer time, around the o-HZO(111) reflection. (c) Vertical and (d) in-plane phase contrast for the HZO/LSMO/STO(001). (e) Vertical and (f) in-plane phase contrast for the HZO/LSMO/STO(110).

The HZO film on LSMO/STO(001) shows the orthorhombic (o) o-HZO(111) peak at  $2\theta \sim 30^\circ$ . A longer time scan around this peak is in Fig 1b. The low intensity peaks at both sides of the o-HZO(111) reflection are Laue oscillations. The thickness of the film, according to the simulation of the peak and Laue fringes (Fig. S1, ESI<sup>†</sup>) is 6.5 nm, and the o-HZO(111) spacing is  $d_{\text{o-HZO}(111)} = 2.972$  Å, matching well with values reported for equivalent films.<sup>10</sup> The scan of the film on LSMO/STO(110) presents an intense o-HZO(111) peak and absence of peaks corresponding to other orientations of the orthorhombic phase or other polymorphs. The o-HZO(111) peak is accompanied of Laue fringes (see the simulation in Fig. S1, ESI<sup>†</sup>). The thickness is 6.5 nm, and the out-of-plane interplanar spacing  $d_{\text{o-HZO}(111)} = 2.946$  Å is slightly lower than that of the film on STO(001). For the film grown on LSMO/STO(001) the vertical and in-plane PFM images show a predominant downwards polarization direction with mixture of in-plane polarization along opposite directions (Fig. 1d) in the as-grown state. Note that the lateral PFM is response has a maximum response when the cantilever lies perpendicular to the polar axis of the film.<sup>24</sup> The film grown on LSMO/STO(110) shows similar vertical and in-plane contrast (Fig. 1d,e). The corresponding amplitude images of Figure 1c-f are shown in Fig. S2, ESI<sup>†</sup>. These results are in agreement with the tilted polarization along [001] direction diagonal with the (111)



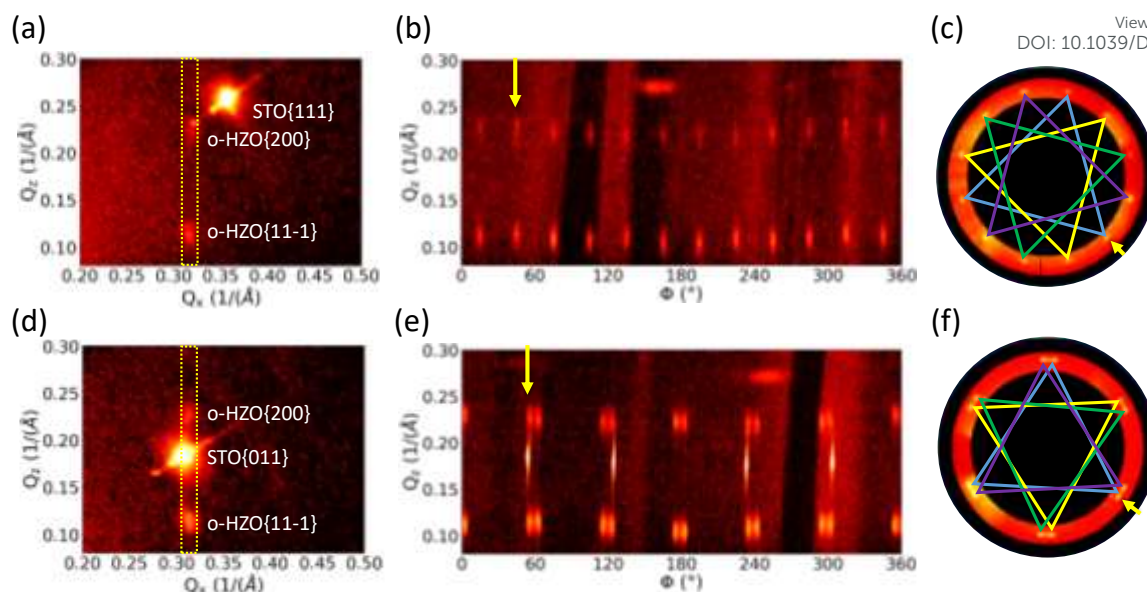


**Fig. 2** (a,d) RSM obtained from processing 2D pole figure frames.  $Q_z$  is the perpendicular component and  $Q_x$  is parallel to the in-plane direction at a specific  $\phi$  angle. The vertical dotted line indicates the position in  $Q_x$  ( $0.314 \pm 0.005 \text{ \AA}^{-1}$ ) that was used to plot in (b,d) the integrated intensity versus  $\phi$ . The yellow arrows indicate the  $\phi$  position of the RSM in (a,d). (c,f) Pole figures corresponding to the o- $\{11-1\}$  planes integrated  $\chi = 71 \pm 7^\circ$  and  $2\theta = 27-33^\circ$ . The triangles are guides to the eye to indicate the four crystallographic o- $\{111\}$  domains. Panels (a-c) and (d-f) correspond to measurements of HZO/LSMO/STO(001) and HZO/LSMO/STO(110), respectively.

texture of the films. It can be also disregarded an important contribution of any (001) texture in the films.

Epitaxy has been studied by XRD using a 2D detector. Fig. 2a shows, for the HZO/LSMO/STO(001) sample, the reciprocal space map (RSM) around the asymmetric STO{111} reflections. The map was obtained from  $\phi$ -scans with 2D detector, recorded at  $\phi$  angles from  $0^\circ$  to  $360^\circ$ , with an step  $\Delta\phi = 1^\circ$ . In addition of the STO{111} spot, the integrated frame shows the presence of a spot that corresponds to o-HZO{11-1} reflections ( $Q_x = 0.316 \text{ \AA}^{-1}$ ,  $Q_z = 0.109 \text{ \AA}^{-1}$ ) and a lower intensity spot of o-HZO{200} reflections ( $Q_x = 0.316 \text{ \AA}^{-1}$ ,  $Q_z = 0.224 \text{ \AA}^{-1}$ ). The presence of both spots at the same  $\phi$  is due to  $180^\circ$  twinning. The diffraction spots appear at specific  $\phi$  angles, as can be seen in Fig. 2b. Fig. 2b shows a  $Q_z - \phi$  map obtained by slicing the RSM around  $Q_x =$

$0.316 \text{ \AA}^{-1}$  ( $\Delta Q = \pm 0.01 \text{ \AA}^{-1}$ ). The integrated region is marked by a box and the corresponding  $\phi$  position is indicated by an arrow in Fig. 2b. There are 12 spots,  $30^\circ$  apart, corresponding to both o-HZO{11-1} and o-HZO{200} reflections. The pole figure of the o-HZO{11-1} reflections in Fig. 2c allows to visualize more clearly the presence of four families of in-plane crystal variants consequence of the epitaxy of o-HZO(111) (3-fold symmetry surface) on LSMO/STO(001) (4-fold symmetry surface).<sup>18</sup> The four families are indicated by colored triangles. Similar measurements for the HZO/LSMO/STO(110) sample are presented in Fig. 2d-f. Fig. 2d shows the RSM around the asymmetric STO{011} reflections. In addition to the substrate spot there are the o-HZO{11-1} ( $Q_x = 0.313 \text{ \AA}^{-1}$ ,  $Q_z = 0.115 \text{ \AA}^{-1}$ ) and o-HZO{200} reflections ( $Q_x = 0.313 \text{ \AA}^{-1}$ ,  $Q_z = 0.225 \text{ \AA}^{-1}$ ). The

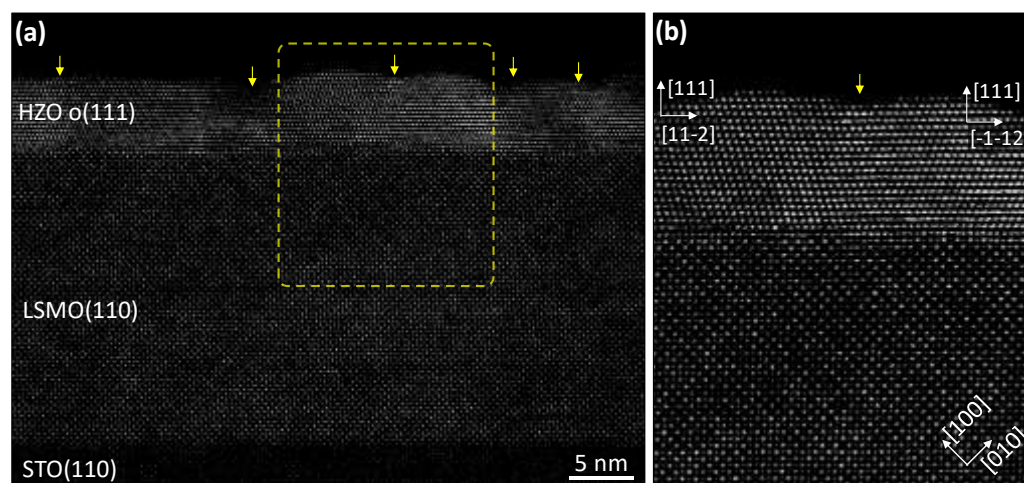


**Fig. 3** (a) Cross-sectional contrast inverted annular bright field image showing, from bottom to top, the STO(110) substrate, the LSMO(110) electrode and the HZO(111) film. The location of the (coherent) boundaries between mirror-like in-plane crystallographic variants are indicated by yellow arrows at the top of the image. (b) Zoomed region showing two orthorhombic HZO grains and part of the LSMO electrode. (b) has been extracted from within the area marked with yellow dashed line in (a).



$Q_z - \phi$  map (Fig. 2e) shows 12 o-HZO{11-1} and 12 o-HZO{200} spots. The 12 spots are distributed in 6 sets of 2 spots, each set about  $60^\circ$  apart and the two spots in each set  $8.5^\circ$  apart. Other heterostructures with complex domain structures have shown similar sets of peaks in  $\phi$ -scans.<sup>25,26</sup> The pole figure in Fig. 2f evidences the angular distribution of the o-HZO{11-1} reflections. The pole figure indicates that there are four HZO crystal domains (Fig. S3, ESI<sup>†</sup>), being the corresponding epitaxial relationships: [-211]HZO(111) // [-112]STO(110), [-211]HZO(111) // [1-12]STO(110), [2-1-1]HZO(111) // [-112]STO(110), and [2-1-1]HZO(111) // [1-12]STO(110).

To better understand epitaxy, we have conducted cross-sectional STEM characterization along the [001] zone axis of STO. Figure 3a shows an inverse-intensity annular bright field (ABF) image where the HZO and LSMO layers and the STO substrate are visualized (horizontal yellow arrows mark the position of the interfaces). Original ABF image and simultaneously acquired high-angle annular dark field images are shown in Fig. S4, ESI<sup>†</sup>. Fig. 3a shows that HZO is orthorhombic, and different crystal variants are observed (vertical yellow arrows mark the position of boundaries between variants). There is absence of monoclinic phase or other HZO polymorphs in Fig. 3a, although monoclinic grains were occasionally observed in other regions of the STEM specimen. Thus, the HZO film on LSMO/STO(110) is almost pure orthorhombic. This is remarkable, since equivalent films on

LSMO/STO(001) show coexistence of orthorhombic and monoclinic phases.<sup>14</sup> The rectangular area marked with a dashed yellow line is shown in an enlarged view in Fig. 3b. The image confirms the high crystalline quality of HZO and shows a well-defined (semi) coherent HZO/LSMO interface. The lattice mismatch, around -11%, is too high for conventional epitaxy. Indeed, comparison of the LSMO(110) and HZO(111) unit cells does not reveal direct matching (Fig. S5, ESI<sup>†</sup>). Domain matching epitaxy, recently observed in the high-mismatch growth of HZO on LSMO(001),<sup>18</sup> is also expected to occur in films grown on LSMO(110). To confirm it, we obtained reconstructed STEM images by filtering in the Fourier space (Fig. S6, ESI<sup>†</sup>). The analysis confirms the presence of extra planes at the HZO/LSMO interface with the periodicity anticipated in domain matching epitaxy. Finally, we note that HZO is (111) oriented on both LSMO(001) and LSMO(110) surfaces. This suggests the relevance of the surface energy contribution in addition of the interface energy. On the other hand, atomic force microscopy measurements confirm that the film of STO(110) is very flat, with root mean square roughness of 0.25 nm (Fig. S7, ESI<sup>†</sup>), which is comparable to the films on STO(001).<sup>10</sup>

Measurements of polarization loops confirm that the HZO films on LSMO/STO(001) and LSMO/STO(110) are ferroelectric (Fig. 4). The current - voltage curve (black line) of the film on STO(001) shows two ferroelectric switching peaks at -2.7 and +1.8 V. The average coercive field ( $E_c$ ) is  $E_c = 3.4 \text{ MV cm}^{-1}$  and there is an internal field of  $1.3 \text{ MV cm}^{-1}$  pointing from the upper Pt contact towards the lower LSMO electrode, as shown by PFM characterization. The polarization loop (Fig. 3b, black line) is well saturated and the remanent polarization ( $P_r$ ) is  $22 \mu\text{C cm}^{-2}$ , similar to the reported values for films of comparable thickness.<sup>10</sup> Fig. 3 also shows the current - voltage curve and the polarization loop of the equivalent film on LSMO/STO(110) (red lines). In this sample, the coercive voltages are -2.3 and +1.9 V, corresponding to an average  $E_c$  of  $3.4 \text{ MV cm}^{-1}$  and internal field of  $0.6 \text{ MV cm}^{-1}$ . The remanent polarization,  $P_r = 33 \mu\text{C cm}^{-2}$ , is much higher than the usual values reported for HZO.<sup>2,3</sup> Remarkably,  $P_r$  is 50% higher than the equivalent epitaxial film grown simultaneously on STO(001). The larger polarization is likely consequence of the higher amount of orthorhombic phase in the film on LSMO/STO(110). The STEM characterization has shown that it is almost pure orthorhombic (Fig. 3), while films on LSMO/STO(001) present an important amount of parasitic monoclinic phase.<sup>14</sup> Theoretical calculations have predicted a spontaneous polarization of 52-55  $\mu\text{C cm}^{-2}$ , for orthorhombic  $\text{HfO}_2$ .<sup>27,28</sup> The projected polarization along the [111] direction of a pure orthorhombic phase film would be around  $31 \mu\text{C cm}^{-2}$ , which is similar to the measured remanent polarization. On the other hand, the HZO film on STO(110) presents a leakage current of about  $5 \times 10^{-7} \text{ A cm}^{-2}$  at  $1 \text{ MV cm}^{-1}$ , slightly less than the about  $1 \times 10^{-6} \text{ A cm}^{-2}$  of the film on STO(001) (Fig. S8, ESI<sup>†</sup>).

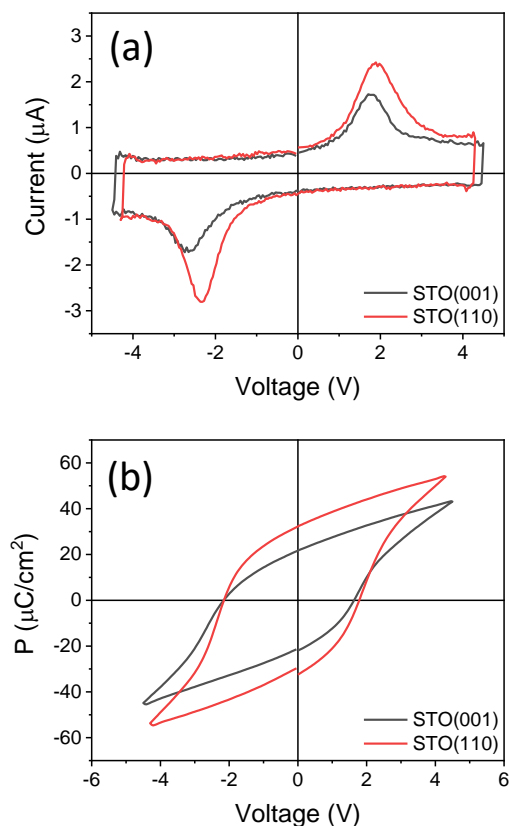


**Fig. 4** (a) Current-voltage curves of the HZO/LSMO/STO(001) (black line) and HZO/LSMO/STO(110) (red line) samples, measured in the pristine state. (b) Corresponding polarization loops.



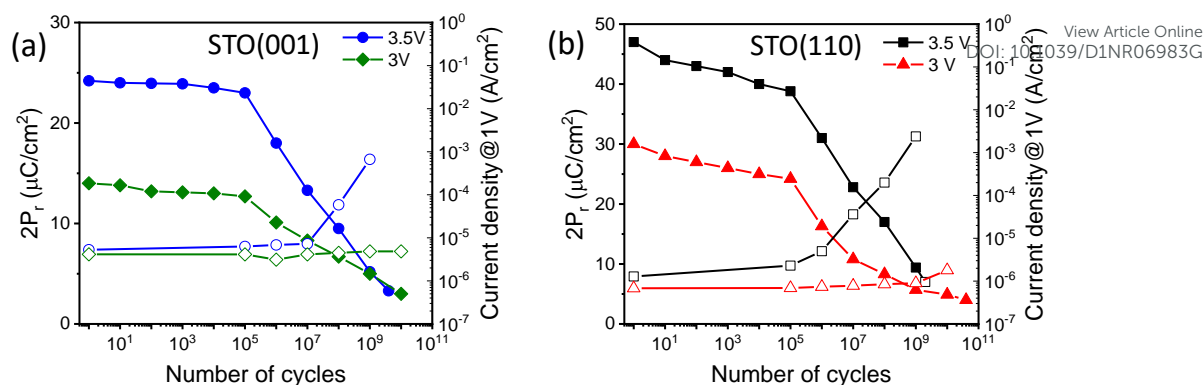


**Fig. 5** (a) Endurance (solid symbols) and current leakage as a function of the number of cycles (empty symbols) of the HZO/LSMO/STO(001) sample cycled by 3.5 V (blue symbols) and 3 V (green symbols). (b) Endurance (solid symbols) and current leakage as a function of the number of cycles (empty symbols) of the HZO/LSMO/STO(110) sample cycled by 3.5 V (black symbols) and 3 V (red symbols).

Fig. 5 shows endurance measurements of the films. The film on STO(001) (Fig. 5a), cycled with sub-coercive field voltage pulses of 3.5 V (electric field  $E = 5.4 \text{ MV cm}^{-1}$ ) having  $2P_r = 24.2 \text{ } \mu\text{C cm}^{-2}$  in pristine state (solid blue circles). There is not significant wake up effect. Polarization does not change significantly after  $10^5$  cycles, but additional cycles cause fatigue. The measurement was stopped when the polarization was as low as  $2P_r = 3.3 \text{ } \mu\text{C cm}^{-2}$  after  $4 \times 10^9$  cycles. The current leakage (open blue circles in Fig. 5a) was constant up to about  $10^7$  cycles, increasing dramatically with additional cycles (see current - voltage curves in Fig. S8, ESI<sup>†</sup>). The test of endurance at 3 V (solid green diamonds) shows a similar dependence. The polarization in pristine state is lower, but the fatigue after  $10^5$  cycles is less pronounced and the capacitor was cycled up to  $10^{10}$  cycles (the test was stopped due to the low  $2P_r$  of  $3 \text{ } \mu\text{C cm}^{-2}$ , see polarization - voltage loops in Fig. S9, ESI<sup>†</sup>). The current leakage (open green diamonds in Fig. 5a) was constant during the test. The film on STO(110), switched at same voltage of 3.5 V (Fig. 5b, solid black squares), has a larger initial polarization,  $2P_r = 47 \text{ } \mu\text{C cm}^{-2}$ . It presents a slight fatigue from the first cycles, being more pronounced after  $10^5$  cycles, and there is breakdown after  $2 \times 10^9$  cycles. The breakdown is likely due to the increased leakage after cycling (open black squares), which was larger

than in the sample grown on STO(110) after  $10^9$  cycles. Reducing the electric field is essential to avoid breakdown. The remanent polarization of the film on STO(110) is very high, and applying a lower voltage, 3 V ( $E = 4.6 \text{ MV cm}^{-1}$ ), the initial polarization,  $2P_r = 30 \text{ } \mu\text{C cm}^{-2}$ , is greater than in the film on STO(001) cycled with 3.5 V pulses. The evolution of polarization with cycling (solid red triangles in Fig. 5b) is similar to that at higher field, but in this case, there is no electrical breakdown up to  $4 \times 10^{10}$  cycles when  $2P_r$  decreased to  $4 \text{ } \mu\text{C cm}^{-2}$  and the measurement was stopped. Polarization fatigue is the main factor that limits endurance in epitaxial HZO films. The robustness against breakdown is probably because the fact that the current leakage (open red triangles in Fig. 5b), contrary to what is observed for 3.5 V cycling voltage, does not increase significantly while cycling.

Fig. 6 shows the retention measurements of the HZO/LSMO/STO(110) sample, after poling a capacitor with pulses of amplitude +3 V (solid triangles) and -3 V (open triangles). The measurements were performed at a temperature of  $85 \text{ } ^\circ\text{C}$ . Dashed red lines are fits to  $P_r = P_0 \cdot \tau_d^{-n}$ , where  $\tau_d$  is the delay time and  $n$  a fitting parameter.<sup>29</sup> The vertical black dashed line indicates a 10 years' time. The extrapolated polarization is high after 10 years for both positive and negative poling at 3 V, the poling amplitude that allows an endurance of  $4 \times 10^{10}$  cycles. Therefore, the film shows high polarization ( $2P_r = 30 \text{ } \mu\text{C cm}^{-2}$ ), endurance ( $4 \times 10^{10}$  cycles) and retention (more than 10 years) under the same poling voltage.

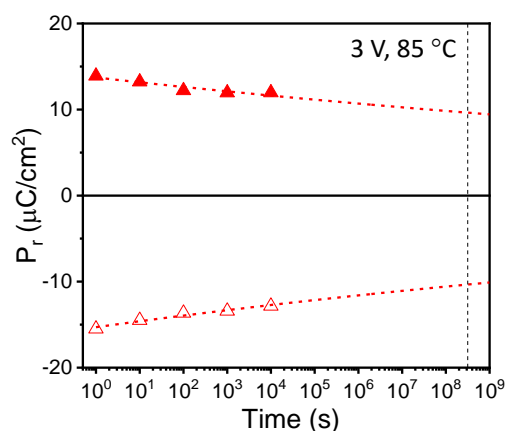


**Fig. 6** Polarization retention measurements at  $85 \text{ } ^\circ\text{C}$  of the HZO/LSMO/STO(110) for positive and negative poling of 3 V. Lines are fits  $P_r = P_0 \cdot \tau_d^{-n}$ .

#### 4. Conclusions

In summary, it is shown that the epitaxial stabilization of the orthorhombic phase of HZO on LSMO/STO(001) also occurs on LSMO/STO(110). HZO films are (111) oriented and have in-plane crystal variants on both substrates, but the variants have different angular distribution. The use of an STO(110) substrate allows the ferroelectric polarization to be increased by 50%, with a high remanent polarization of  $33 \text{ } \mu\text{C cm}^{-2}$  in a film of less than 7 nm. The high polarization is accompanied by a very large endurance ( $4 \times 10^{10}$  cycles) and retention extrapolated to more than 10 years. The results point out that adjusting the epitaxial



growth, here carried out by orientation of the substrate, can allow a further improvement of the properties.

### Conflicts of interest

There are no conflicts to declare.

### Acknowledgements

Financial support from the Spanish Ministry of Science and Innovation, through the Severo Ochoa FUNFUTURE (CEX2019-000917-SMCIN, AEI/10.13039/501100011033), PID2020-112548RB-I00 (MCIN/AEI/10.13039/501100011033) and PID2019-107727RB-I00 (MCIN/AEI/10.13039/501100011033) projects, from CSIC through the i-LINK (LINKA20338) program, and from Generalitat de Catalunya (2017 SGR 1377) is acknowledged. Project supported by a 2020 Leonardo Grant for Researchers and Cultural Creators, BBVA Foundation. IF acknowledges Ramón y Cajal contract RYC-2017-22531. TS and HT are financially supported by China Scholarship Council (CSC) with No. 201807000104, and 201906050014. TS and HT work has been done as a part of their Ph.D. program in Materials Science at Universitat Autònoma de Barcelona.

### References

- 1 T. S. Böscke, J. Müller, D. Bräuhäus, U. Schröder and U. Böttger, *Appl. Phys. Lett.*, 2011, **99**, 102903.
- 2 I. Fina and F. Sánchez, *ACS Appl. Electron. Mater.*, 2021, **3**, 1530.
- 3 J. Cao, S. Shi, Y. Zhu and J. Chen, *Phys. status solidi – Rapid Res. Lett.*, 2021, **15**, 2100025.
- 4 T. Shimizu, K. Katayama, T. Kiguchi, A. Akama, T. J. Konno, O. Sakata and H. Funakubo, *Sci. Rep.*, 2016, **6**, 32931.
- 5 J. Lyu, I. Fina, R. Solanas, J. Fontcuberta and F. Sánchez, *Appl. Phys. Lett.*, 2018, **113**, 082902.
- 6 Y. Wei, P. Nukala, M. Salverda, S. Matzen, H. J. Zhao, J. Momand, A. S. Everhardt, G. Agnus, G. R. Blake, P. Lecoeur, B. J. Kooi, J. Íñiguez, B. Dkhil and B. Noheda, *Nat. Mater.*, 2018, **17**, 1095.
- 7 Z. Zhang, S. Hsu, V. A. Stoica, H. Paik, E. Parsonnet, A. Qualls, J. Wang, L. Xie, M. Kumari, S. Das, Z. Leng, M. McBriarty, R. Proksch, A. Gruverman, D. G. Schlom, L. Chen, S. Salahuddin, L. W. Martin and R. Ramesh, *Adv. Mater.*, 2021, **33**, 2006089.
- 8 J. Lyu, T. Song, I. Fina and F. Sánchez, *Nanoscale*, 2020, **12**, 11280.
- 9 T. Shimizu, T. Mimura, T. Kiguchi, T. Shiraishi, T. Konno, Y. Katsuya, O. Sakata and H. Funakubo, *Appl. Phys. Lett.*, 2018, **113**, 212901.
- 10 J. Lyu, I. Fina, R. Solanas, J. Fontcuberta and F. Sánchez, *ACS Appl. Electron. Mater.*, 2019, **1**, 220.
- 11 T. Song, R. Bachelet, G. Saint-Girons, R. Solanas, I. Fina and F. Sánchez, *ACS Appl. Electron. Mater.*, 2020, **2**, 3221.
- 12 T. Song, R. Bachelet, G. Saint-Girons, N. Dix, I. Fina and F. Sánchez, *J. Mater. Chem. C*, 2021, **9**, 12224.
- 13 T. Mimura, T. Shimizu, Y. Katsuya, O. Sakata and H. Funakubo, *Jpn. J. Appl. Phys.*, 2020, **59**, SGG04.
- 14 S. Estandía, N. Dix, J. Gazquez, I. Fina, J. Lyu, M. F. Chisholm, J. Fontcuberta and F. Sánchez, *ACS Appl. Electron. Mater.*, 2019, **1**, 1449.
- 15 T. Song, S. Estandía, H. Tan, N. Dix, J. Gàzquez, I. Fina and F. Sánchez, *Adv. Electron. Mater.*, 2021, 2100420.
- 16 D. G. Schlom, L. Q. Chen, C. B. Eom, K. M. Rabe, S. K. Streiffer and J. M. Triscone, *Annu. Rev. Mater. Res.*, 2007, **37**, 589.
- 17 L. W. Martin and A. M. Rappe, *Nat. Rev. Mater.*, 2017, **2**, 16087.
- 18 S. Estandía, N. Dix, M. F. Chisholm, I. Fina and F. Sánchez, *Cryst. Growth Des.*, 2020, **20**, 3801.
- 19 S. Estandía, J. Gàzquez, M. Varela, N. Dix, M. Qian, R. Solanas, I. Fina and F. Sánchez, *J. Mater. Chem. C*, 2021, **9**, 3486.
- 20 J. Lyu, I. Fina and F. Sánchez, *Appl. Phys. Lett.*, 2020, **117**, 072901.
- 21 R. Meyer, R. Waser, K. Prume, T. Schmitz and S. Tiedke, *Appl. Phys. Lett.*, 2005, **86**, 142907.
- 22 S. González-Casal, I. Fina, F. Sánchez and J. Fontcuberta, *ACS Appl. Electron. Mater.*, 2019, **1**, 1937.
- 23 B. J. Rodriguez, C. Callahan, S. V. Kalinin and R. Proksch, *Nanotechnology*, 2007, **18**, 475504.
- 24 E. Gradauskaitė, N. Gray, M. Campanini, M. D. Rossell and M. Trassin, *Chem. Mater.*, 2021, **33**, 9439.
- 25 H. N. Lee, D. Hesse, N. Zakharov and U. Gösele, *Science*, 2002, **296**, 2006.
- 26 J. Roldán, F. Sánchez, V. Trtik, C. Guerrero, F. Benitez, C. Ferrater and M. Varela, *Appl. Surf. Sci.*, 2000, **154–155**, 159.
- 27 T. D. Huan, V. Sharma, G. A. Rossetti and R. Ramprasad, *Phys. Rev. B*, 2014, **90**, 064111.
- 28 F. Delodovici, P. Barone and S. Picozzi, *Phys. Rev. Mater.*, 2021, **5**, 064405.
- 29 D. J. Kim, J. Y. Jo, Y. S. Kim, Y. J. Chang, J. S. Lee, J.-G. Yoon, T. K. Song and T. W. Noh, *Phys. Rev. Lett.*, 2005, **95**, 237602.

